OPEN

Vestibular Aqueduct Morphology Correlates With Endolymphatic Sac Pathologies in Menière's Disease—A Correlative Histology and Computed Tomography Study

*†David Bächinger, ‡§Ngoc-Nhi Luu, ‡§Judith S. Kempfle, ‡§Samuel Barber, ||Daniel Zürrer, ‡§Daniel J. Lee, §¶Hugh D. Curtin, §#Steven D. Rauch, §**Joseph B. NadolJr., §**Joe C. Adams, and §**†Andreas H. Eckhard

*Department of Otorhinolaryngology, Head and Neck Surgery, University Hospital Zurich; †University of Zurich, Zurich, Switzerland; ‡Eaton-Peabody Laboratories, Eye and Ear Infirmary; §Department of Otolaryngology, Harvard Medical School; ||Independent Researcher, Zurich, Switzerland; ¶Department of Radiology; #Vestibular Division, Department of Otolaryngology, Massachusetts Eye and Ear Infirmary and Massachusetts General Hospital; and **Otopathology Laboratory, Department of Otolaryngology, Massachusetts Eye and Ear Infirmary, Boston, Massachusetts

Hypothesis: The vestibular aqueduct (VA) in Menière's disease (MD) exhibits different angular trajectories depending on the presenting endolymphatic sac (ES) pathology, i.e., 1) ES hypoplasia or 2) ES degeneration.

Background: Hypoplasia or degeneration of the ES was consistently found in inner ears affected by MD. The two etiologically distinct ES pathologies presumably represent two disease ''endotypes,'' which may be associated with different clinical traits (''phenotypes'') of MD. Recognizing these endotypes in the clinical setting requires a diagnostic tool.

Methods: 1) Defining the angular trajectory of the VA (ATVA) in the axial plane. 2) Measuring age-dependent normative data for the ATVA in postmortem temporal bone histology material from normal adults and fetuses. 3) Validating ATVA measurements from normative CT imaging data. 4) Correlating the ATVA with different ES pathologies in histological materials and CT imaging data from MD patients.

Results: 1) The ATVA differed significantly between normal adults and MD cases with ES degeneration, as well as between fetuses and MD cases with ES hypoplasia; 2) a strong correlation between ATVA measurements in histological sections and CT imaging data was found; 3) a correlation between the ATVA, in particular its axial trajectory in the opercular region (angle α_{exit}), with degenerative ($\alpha_{exit} < 120^{\circ}$) and hypoplastic ES pathology ($\alpha_{exit} > 140^{\circ}$) was demonstrated.

Conclusion: We established the ATVA as a radiographic surrogate marker for ES pathologies. CT-imaging-based determination of the ATVA enables endotyping of MD patients according to ES pathology. Future studies will apply this method to investigate whether ES endotypes distinguish clinically meaningful subgroups of MD patients. **Key Words:** Computed tomography—Endolymphatic sac—Endotype—Menière—Vestibular aqueduct.

Otol Neurotol **40:**e548–e555, 2019.

Patients with Menière's disease (MD) demonstrate a high degree of interindividual variability in the presentation of audiovestibular symptoms (1,2). This variability has previously raised the questions of whether

Address correspondence and reprint requests to Andreas H. Eckhard, M.D., Department of Otorhinolaryngology, University Hospital Zurich, Frauenklinikstrasse 24, 8091 Zurich, Switzerland; E-mail: AndreasHeinrich.Eckhard@usz.ch

Author contributions: J.C.A. and A.H.E. conceived and designed the study. D.Z. and D.B. designed the software for angle measurements. D.B. and N.L. conducted the measurements. D.B., S.B., and A.H.E. prepared the figures and wrote the manuscript. J.S.K., D.J.L., and H.D.C. provided CT imaging data from clinical cases. J.S.K., D.J.L., S.D.R., J.C.N., and J.C.A. provided critical review of the manuscript.

This work was supported by grants from the American Hearing Research Foundation and the GEERS Foundation (S030 – 10.051). The author AHE was supported by a Research fellowship grant (EC 472/1) from the German Research Council (Deutsche Forschungsgemeinschaft). The author DB was supported by a Graduate Campus Travel Grant from the University of Zurich, Switzerland. The author NL was supported by an Emerging Research Grant from the Hearing Health foundation.

The authors disclose no conflicts of interest.

Supplemental digital content is available in the text.

DOI: 10.1097/MAO.0000000000002198

distinct disease phenotypes exist among patients and whether those phenotypes are caused by different endotypes—i.e., different pathologies affecting the inner ear (2,3). A recent human pathology study (4) was the first to demonstrate two etiologically distinct inner ear pathologies (suspected endotypes) that both affect the endolymphatic sac (ES) (Fig. 1A) and are ubiquitously present among MD patients: 1) degenerative change in the ES (54.2% of cases) and 2) developmental hypoplasia of the ES (37.5% of cases). Correlations with clinical record data suggest that these ES pathologies (endotypes) are associated with different clinical traits (phenotypes). To further investigate the presence of discrete endotype–phenotype patterns based on ES pathologies in patients, clinically applicable methods are necessary to distinguish degenerative versus hypoplastic ES pathology.

Here, we used postmortem temporal bone sections from MD cases and CT imaging data from clinical

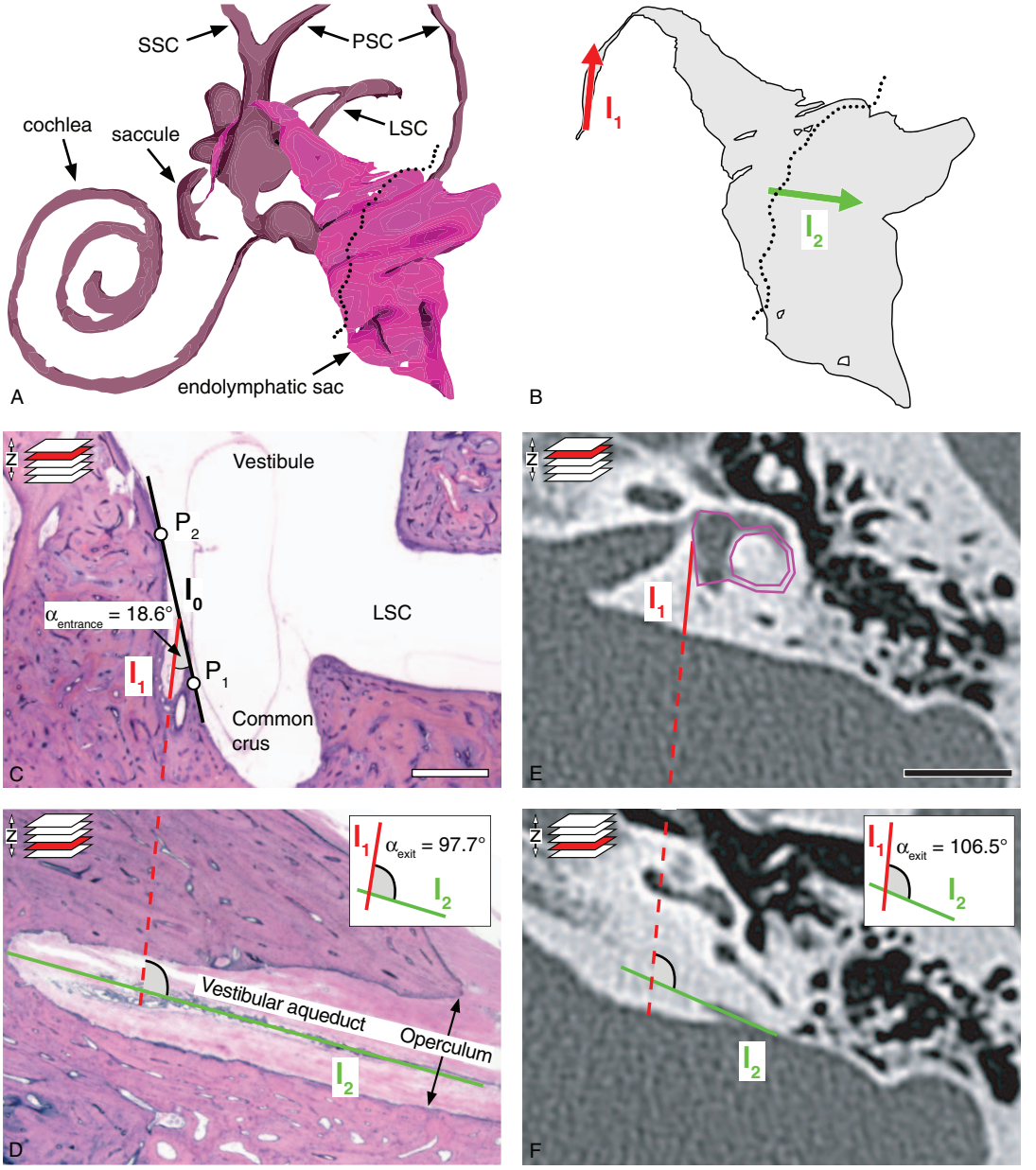

FIG. 1. Methods to determine $\alpha_{entrance}$ and α_{exit}, i.e., the angular trajectory of the vestibular aqueduct (ATVA), in histological sections and CT images. *A*, 3D reconstruction of the endolymphatic space of a human (normal adult) inner ear. The dotted line indicates the opening of the opercular region. *B*, Endolymphatic duct and endolymphatic sac. Lines l_1 (red) and l_2 (green) used for assessing α_{exit} are indicated. *C* and *D*, Histological assessment of α_{exit} in a normal adult temporal bone. *E* and *F*, Software-based method to determine α_{exit} from temporal bone CT images. See text for details. Scale bars: (*D* and *E*) 1 cm. CT indicates computed tomography; LSC, lateral semicircular canal; PSC, posterior semicircular canal; SCC, superior semicircular canal. Images of 3D models for *A* and *B* have been adapted from the 3D temporal bone model of the Eaton-Peabody Laboratory Massachusetts Eye and Ear Infirmary, Boston, MA (5).

TABLE 1. *Groups of cases and patients*

Study Groups	Specimens (Cases)	Modality	Age in Years (Mean ± SD), Except for Fetuses	Sex Distribution (Males, Females)
Normal adults (pathology cases)	46 (43)	Histology	55.8 ± 22.3^a	25 (58.1%), 18 (41.9%)
Normal adults (pathology cases) with available CT scans	16 (9)	Histology and CT	74.6 ± 17.0^a	4 (44.4%), 5 (55.6%)
Normal adults (clinical patients)	64 (35)	CT	47.7 ± 16.5^b; $p = 0.18^c$	16 (45.7%), 19 (54.3%); $p = 0.27$
Fetuses (pathology cases)	44 (22)	Histology	Range: 6–38 weeks	n.a.
MD, degenerated ES (pathology cases)	18 (16)	Histology	76.5 ± 20.1^a	4 (25.0%), 12 (75.0%)
MD, hypoplastic ES (pathology cases)	14 (9)	Histology	82.9 ± 11.2^a	6 (66.7%), 3 (33.3%)

[a]At time of death.
[b]At time of CT scan.
[c]*P*-value of difference between normal adult pathology cases (histology) and normal adult clinical cases (CT).
ES indicates endolymphatic sac; MD, Menière's disease; n.a., data not available.

MD patients to investigate whether different ES pathologies (degeneration versus hypoplasia) are associated with different angular trajectories of the vestibular aqueduct (ATVAs) in the temporal bone. The goal of this study was to establish the ATVA as a radiographic marker to distinguish degenerative from hypoplastic ES pathology in clinical MD patients.

MATERIALS AND METHODS

Ethics

This study was approved by the institutional Review Board of the Massachusetts Eye and Ear Infirmary (IRBNet-ID 880454-1; Boston, MA).

Archival Human Temporal Bone Specimens

From the human pathology collection at the Massachusetts Eye and Ear Infirmary, a total of 136 temporal bone specimens were included from cases with normal age-related audiometric threshold patterns and no history of otologic disease (n = 62), fetuses (abortion samples) with no histological signs of developmental defects (n = 42), and cases with a clinical diagnosis of definite MD (n = 32) (Table 1). All specimens were processed for light microscopy using previously described methods (6).

Temporal Bone CT Imaging Data From Archival Specimens and From Clinical Patients

CT scans of postmortem temporal bone specimens were obtained after tissue removal and fixation and before decalcification, using standard protocols for dedicated high-resolution temporal bone imaging. High-resolution or cone-beam CT imaging of the temporal bones from clinical patients (n = 35; Table 1), all of whom were scanned for suspected diseases not related to the inner ear, was performed without intravenous contrast. All data were reconstructed separately for each temporal bone in the axial plane by using a standard bone algorithm.

Endolymphatic Sac Histopathologies in MD

The histological criteria for degenerative and hypoplastic ES pathology have been described previously (4). Briefly, in degenerative ES pathology, the epithelium in the distal (extraosseous) ES portion exhibits degenerative changes, i.e., pycnotic nuclei, expelled/missing cells, and fibrotic replacement. In hypoplastic ES pathology, the ES is not properly developed and lacks an extraosseous portion.

All specimens with degenerative (n = 18) and hypoplastic ES pathology (n = 14) that were used in the present study have been previously characterized (4).

ATVA Measurements in Histological Sections

The ATVA was determined in horizontally sectioned temporal bone specimens by measuring 1) the entrance trajectory (red arrow, Fig. 1B) of the proximal VA portion into the temporal bone (angle ''$\alpha_{entrance}$'') and 2) the trajectory along which the VA exits the temporal bone (green arrow, Fig. 1B) in the opercular region (angle ''α_{exit}''). To determine $\alpha_{entrance}$ (Fig. 1C), we used two points (P_1 and P_2) on the medial wall of the vestibule, with a distance to the internal orifice of the VA of approximately 1 mm, to define a line l_0. A second line l_1 was set to run across the orifice, parallel to the most proximal part of the VA. $\alpha_{entrance}$ is the acute angle enclosed by the lines l_0 and l_1. α_{exit} was determined in a different, more caudally located section plane in the opercular region (Fig. 1D). Here, a line l_2 was placed parallel to the most distal part of the VA. α_{exit} is the angle enclosed by lines l_1 from Figure 1C and l_2, which were merged in a virtual plane (Fig. 1D, inset). $\alpha_{entrance}$ was measured using the angle measurement tool of the software Fiji (7). α_{exit} was determined using a custom-designed software (see next paragraph and PDF file, Supplemental Digital Content 1, http://links.lww.com/MAO/A755).

ATVA Measurements in CT Images

We modified the method used on histological sections (previous paragraph) for ATVA measurements, since, due to the limits of image resolution, CT did not provide reliable visualization of the VA at its origin from the vestibule. Hence, $\alpha_{entrance}$ could not be determined in CT images. Instead, a predefined shape (magenta shape, Fig. 1E) was congruently fitted into the bony boundaries of the vestibule and the lateral semicircular canal in the appropriate image plane. The proportions of the shape were determined on an axial CT image from a normal adult temporal bone in which the entire vestibule and lateral semicircular canal were visible. Fitting this shape to more than 100 CT image data sets in this study required only very minor adjustments to the shape's side ratios, confirming its overall good fit to the normal adult temporal bone anatomy. The line l_1 was attached to this shape at a fixed angle of 14.0 degrees, representing the average α_{exit}, as determined from histological sections from normal adult controls (see Results section). Analogous to the method used on histological sections, a line l_2 was set to run parallel to the most distal part of the VA in the opercular region in a more caudally located image plane (Fig. 1F). α_{exit} is the angle between lines l_1 and l_2 (Fig. 1F, inset).

Software for ATVA Measurements

A custom-made open-source web application was developed for angle measurements from CT imaging data. The software is freely available for download at https://github.com/DanielZuerrer/CoolAngleCalcJS or as an online version at

https://danielzuerrer.github.io/CoolAngleCalcJS. An illustrated step-by-step manual for angle measurements is provided as digital supplemental material (Supplemental Digital Content 1, http://links.lww.com/MAO/A755).

Statistical Analysis

Statistical analysis was performed using the software Prism (version 7.0a; GraphPad Software Inc., La Jolla, CA). For group comparisons, one-way analysis of variance was performed, along with post hoc multiple comparison testing by the Holm–Sidak method. For comparison of α_{exit} (CT images and histological sections) from adult controls, Student's unpaired two-sample t test was used. Pearson's correlation coefficient (r) was determined to assess correlations between values for the α_{exit} as determined from histological sections and CT images from adult controls. For all angles, mean values, and standard deviations are reported. The significance level was set to $p < 0.05$.

RESULTS

The ATVA in Temporal Bone Histology: Normal Adults and Fetuses

Normative data for the ATVA ($\alpha_{entrance}$ and α_{exit}) were determined from histological temporal bone sections. $\alpha_{entrance}$ did not differ significantly between normal adults (2D-reconstructed course of a representative VA, Fig. 2A) and fetuses (Fig. 2B) (adults: 14.3 ± 3.8 degrees, range 7.6–22.6 degrees, n = 62; fetuses: 15.6 ± 6.2 degrees, range 4.5–27.8 degrees, n = 42; $p = 0.67$; Fig. 2E). In contrast, α_{exit} was significantly narrower in normal adults than in fetuses (adults: 102.3 ± 9.8 degrees, range, 76.8–119.1 degrees, n = 62; fetuses: 161.5 ± 14.3 degrees, range, 136.6–188.3 degrees, n = 42; $p < 0.0001$; Fig. 2F). In fetuses, no significant correlation was found between α_{exit} and gestational age ($p = 0.10$).

The ATVA in Temporal Bone Histology: Cases With Menière's Disease

In endotyped MD cases (representative VA morphologies shown in Fig. 2C and D) $\alpha_{entrance}$ was determined from histological sections. $\alpha_{entrance}$ was not significantly different between the two groups (degenerated ES: 13.8 ± 4.1 degrees, range, 6.0–21.1 degrees, n = 18; hypoplastic ES: 14.0 ± 3.4 degrees, range, 7.2–19.8 degrees, n = 14; $p = 0.97$), and neither group significantly differed from normal adults or fetuses (Fig. 2F). In contrast, α_{exit} was significantly different between the two MD groups (degenerated ES: 98.9 ± 9.8 degrees, range, 77.5–117.7 degrees, n = 18; hypoplastic ES: 155.6 ± 11.9 degrees, range,

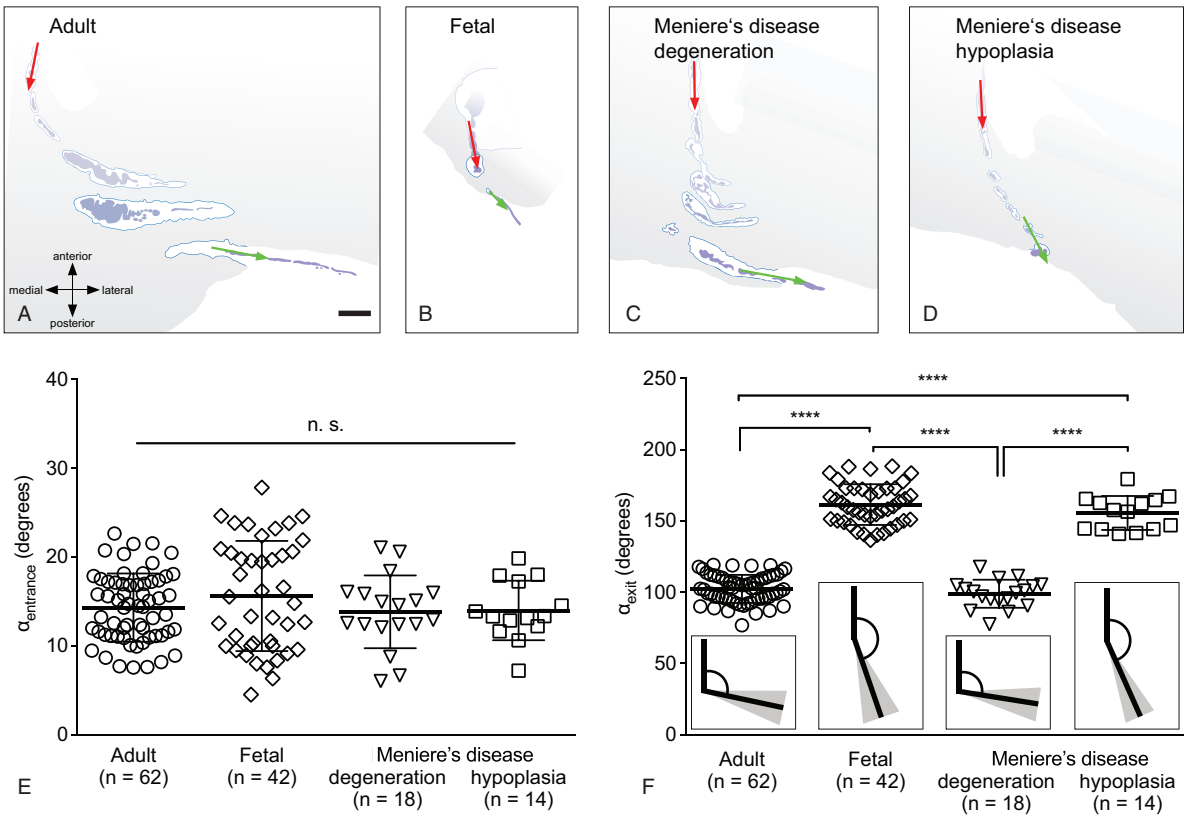

FIG. 2. Angular trajectory of the vestibular aqueduct (ATVA, i.e., $\alpha_{entrance}$ and α_{exit}) measurement in normal adults, fetuses, and Menière's disease (MD) cases. (*A–D*) 2D-reconstructed course of the right vestibular aqueduct from multiple (3–6) histological sections in a normal adult case (79 years; *A*), a fetus (gestational week 8; *B*), an MD case with a degenerated endolymphatic sac (ES) (94 yr; *C*), and an MD case with a hypoplastic ES (97 yr; *D*). (*E* and *F*) Values of $\alpha_{entrance}$ (*E*) and α_{exit} (*F*) in normal adults, fetuses, and MD cases (degenerated ES, hypoplastic ES). Insets in (*F*) illustrate the mean angle (*black lines*) and the corresponding standard deviations (*gray-shaded areas*). Statistics: $^{****}p < 0.0001$; CT indicates computed tomography; n.s., not significant. Scale bar: (*A–D*) 1 mm.

140.9–179.3 degrees, n = 14; $p < 0.0001$). Similar values for α_{exit} (no statistical significance) were found between MD cases (degenerated ES) and normal adults, as well as between MD cases (hypoplastic ES) and fetuses (Fig. 2F).

Correlating the ATVA Between Histology and CT: Normal Adults

To validate ATVA measurements in CT imaging data, we first compared values for α_{exit} determined in temporal bone sections from a group of normal adult cases with values determined in CT images from an unrelated group (no significant age or sex differences, Table 1) and found no significant differences (histology: 102.3 ± 9.8, range, 76.8–119.1, n = 62, data shown in Fig. 2F; CT: 99.9 ± 9.1 degrees, range, 80.0–117.3 degrees, n = 64; $p = 0.21$; Fig. 3A). Next, we determined α_{exit} from 16 temporal bone specimens that were scanned before histological processing. Values determined from CT images and the corresponding histological sections showed a strong correlation ($r = 0.78$, $p = 0.0003$; Fig. 3B).

Correlating the ATVA Between Histology and CT: Cases With Menière's Disease

To investigate whether the ATVA can be determined in MD cases with degenerative versus hypoplastic ES pathology, we used three postmortem temporal bone specimens from two MD cases that underwent CT imaging before histological processing. Histology demonstrated unilateral degenerative pathology in the first case (Fig. 4A) and bilateral hypoplastic ES pathology in the second case (Fig. 4B). Measurements of α_{exit} in both modalities (degenerated ES: Fig. 4C and D; hypoplastic ES: Fig. 4E and F) yielded very similar results with discrepancies of less than 10 degrees (histology – degenerated ES: 87.0 degrees; histology – hypoplastic ES: 165.5 degrees on the left side and 144.6 degrees on the right side; CT – degenerated ES: 88.3 degrees; CT – hypoplastic ES: 160.6 degrees on the left side and 153.6 degrees on the right side; Fig. 4G).

DISCUSSION

Numerous previous studies have attempted to identify disease-specific morphological alterations of the VA in MD based on intraoperative anatomy (8), postmortem histology (9–11), CT imaging (12–17), or MRI (18–21). However, those studies did not consider distinct etiologies (endotypes) of MD or their potentially different effects on VA morphology. Moreover, those previous studies that used clinical imaging (CT/MRI) required elaborate postprocessing methods (e.g., 3D reconstructions, (22)) to determine morphological parameters of the VA.

Here, we established the ATVA, in particular the angle α_{exit}, as a surrogate marker of ES pathologies (histopathological endotypes) in MD (Table 2). By correlating ATVA measurements from histologically processed temporal bones and from CT imaging data, we demonstrated that the ATVA can be reliably determined using clinical imaging data. Our measurements indicated 1) no significant differences in the trajectory of the proximal VA portion ($\alpha_{entrance}$) among all investigated groups, 2) a significant change in the trajectory of the distal VA portion (α_{exit}) between the fetal and adult stages of normal temporal bone development, 3) a similar (no significant difference) α_{exit} between fetal cases and MD cases with hypoplastic ES pathology, and 4) a similar (no significant difference) α_{exit} between normal adult cases and MD cases with degenerative ES pathology.

The observed changes in VA morphology (angle α_{exit}) during ontogenesis (fetal versus adult VA; [(23), present study]) and between MD endotypes (degenerative versus hypoplastic ES pathology; present study) may be attributable to temporal and spatial differences in bone growth

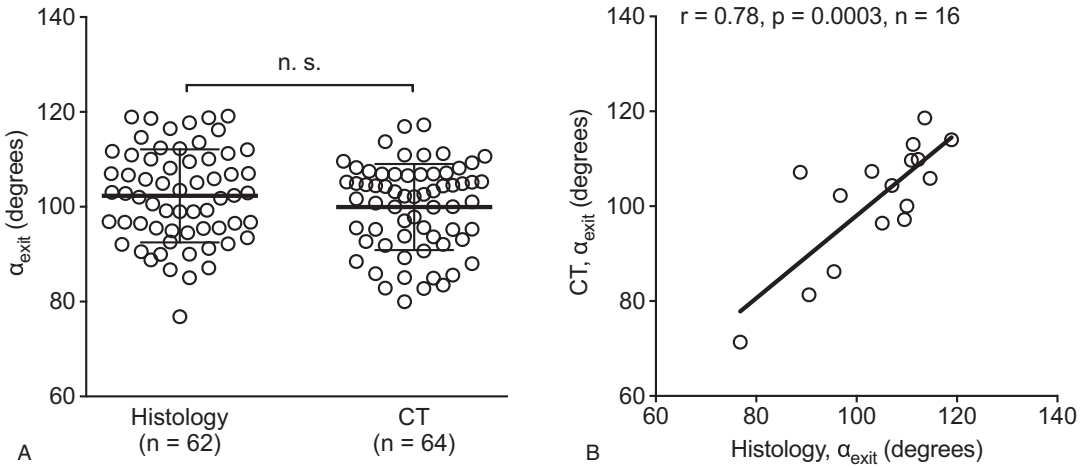

FIG. 3. Normal α_{exit} assessed in histology and CT imaging data. *A*, α_{exit} as determined in two independent groups (first group: histology; second group: CT images). *B*, Correlation of angle values as determined from histological sections and CT images derived from the same temporal bone specimens. CT indicates computed tomography; n.s., not significant.

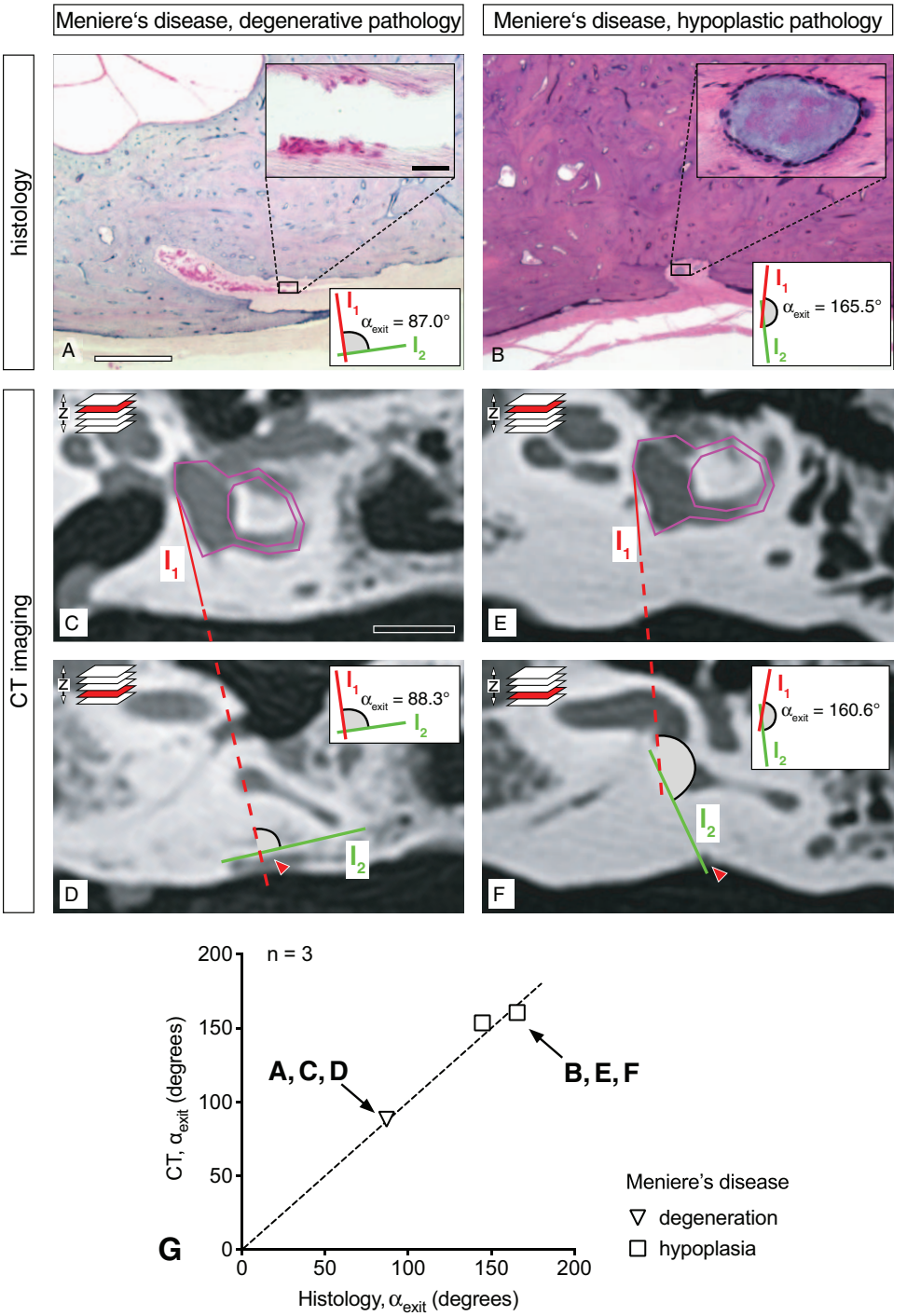

FIG. 4. Correlation of endolymphatic sac (ES) pathology and α_{exit} (histology and CT imaging) in Menière's disease (MD). *A* and *B*, Histological sections (opercular region) from a case of degenerative ES pathology (*A*; inset: degenerated ES epithelium) and a case of hypoplastic ES pathology (*B*; inset: cyst-like distal end of the ES). (*C–F*) CT images from the same specimens as in (*A*) and (*B*) in the axial focal plane of the opercular region. (*E*) Correlation of values for the α_{exit} as determined in CT images and histological sections from the same specimens (n = 3, from two MD cases). Dashed line indicates 100% correlation ($r = 1$); scale bars: (*A–B*) 1 mm, inset in (*A–B*) 50 μm, (*C–D*) 10 mm. Red arrows in (*C–F*) indicate the opercular region. CT indicates computed tomography.

TABLE 2. *Proposed endolymphatic sac pathology-based endotyping*

Clinical Diagnosis	Disease Laterality[a]	α_{exit} (Affected/Non-Affected)	Endotype Diagnosis
Definite Menière's disease	Unilateral	>140 degrees/<120 degrees	Unilateral hypoplastic
		<120 degrees/<120 degrees	Unilateral degenerative, bilateral degenerative[b]
		>140 degrees/>140 degrees	Bilateral hypoplastic[b]
	Bilateral	<120 degrees/<120 degrees	Bilateral degenerative
		>140 degrees/>140 degrees	Bilateral hypoplastic

[a]At time of study.
[b]With initial unilateral clinical presentation.

and development of the petrous bone. The definite size and shape of the bony labyrinth during ontogenesis is thought to be strongly influenced by a decline in the rate of bone metabolism (bone remodeling) in the otic capsule (24), which occurs around the 23rd fetal week (25). At that time point, cells of the membranous labyrinth are presumably starting to secret osteoprotegerin (OPG), an inhibitor of osteoclast activity, into the perilymphatic fluid spaces, from which the OPG diffuses into the surrounding bone (limited by the diffusion gradient) to inhibit bone matrix remodeling (24). Notably, the distal portion of the VA—which undergoes significant morphological changes between the 19th and 23rd fetal week ((23,25), present study)—extends beyond the otic capsule and passes through a layer of normally remodeling (lamellar) bone to the operculum. Prolonged bone growth and continuous bone remodeling in the opercular region during the postnatal period can explain the delayed morphological maturation of the distal VA (compared with the rest of the bony labyrinth), as well as its highly variable morphology in the adult stage (22,26–28).

In the present study, we found that different MD endotypes were associated with significantly different VA morphologies and that the latter resembled very different morphological stages during normal temporal bone development. Hypoplastic ES pathology was associated with an abnormally short, straight VA ($\alpha_{exit} > 140^{\circ}$), as found in fetal (gestational weeks 6–38) developmental stages. This premature VA morphology, together with a hypoplastic ES, supports a genetic/developmental etiology in this endotype, as proposed by Eckhard et al. (4). With α_{exit} consistently more than 140 degrees, we defined a specific imaging-based diagnostic criterion for this endotype. In contrast, the normal (mature) VA morphology in MD cases with degenerative ES pathology suggests an etiology that manifests in adult life and that causes progressive ES degeneration (but does not affect the VA) (4). The range for the angle α_{exit} in this MD endotype was similar to the range observed in normal (adult) morphology. Hence, α_{exit} does not provide a specific diagnostic criterion for this endotype.

In conclusion, determining the ATVA (α_{exit}) from clinical imaging data enables endotyping of MD patients according to the underlying ES pathology. This approach will be applied in future studies to stratify MD patients according to their endotype and to elucidate whether those endotypes determine clinically meaningful, i.e., phenotypically different, patient subgroups.

Acknowledgments: The authors are grateful for the exceptional technical expertise of Barbara Burgess, Diane Jones, Jennifer O'Malley, and MengYu Zhu in preparing the human temporal bone specimens. They also thank Reef Al-Asad for the technical assistance in angle measurements.

REFERENCES

1. Friberg U, Stahle J, Svedberg A. The natural course of Meniere's disease. *Acta Otolaryngol Suppl* 1984;406:72–7.
2. Rauch S. Clinical hints and precipitating factors in patients suffering from Meniere's disease. *Otolaryngol Clin North Am* 2010;43:1011–7.
3. Merchant SN, Adams JC, Nadol JB. Pathophysiology of Meniere's syndrome: are symptoms caused by endolymphatic hydrops? *Otol Neurotol* 2005;26:74–81.
4. Eckhard AH, Zhu M, O'Malley JT, et al. Inner ear pathologies impair sodium-regulated ion transport in Meniere's disease. *Acta Neuropathol* 2019;137:343–57.
5. Wang H, Northrop C, Burgess B, Liberman MC, Merchant SN. Three-dimensional virtual model of the human temporal bone: a stand-alone, downloadable teaching tool. *Otol Neurotol* 2006;27:452–7.
6. Merchant SN, Nadol JB. *Schuknecht's Pathology of the Ear. 3rd ed.*. USA: People's Medical Pub. House; 2010.
7. Schindelin J, Arganda-Carreras I, Frise E, et al. Fiji: an open-source platform for biological-image analysis. *Nat Methods* 2012;9:676–82.
8. Kitahara T, Yamanaka T. Identification of operculum and surgical results in endolymphatic sac drainage surgery. *Auris Nasus Larynx* 2017;44:116–8.
9. Sando I, Ikeda M. The vestibular aqueduct in patients with Meniere's disease: a temporal bone histopathological investigation. *Acta Otolaryngol* 1984;97:558–70.
10. Ikeda M, Sando I. Endolymphatic duct and sac in patients with Meniere's disease: a temporal bone histopathological study. *Ann Otol Rhinol Laryngol* 1984;93:540–6.
11. Yuen SS, Schuknecht HF. Vestibular aqueduct and endolymphatic duct in Meniere's disease. *Arch Otolaryngol* 1972;96:553–5.
12. Clemis JD, Valvassori GE. Recent radiographic and clinical observations on the vestibular aqueduct (a preliminary report). *Otolaryngol Clin North Am* 1968;1968:339–46.
13. Emery PJ, Gibson WR, Lloyd GA, Phelps PD. Polytomography of the vestibular aqueduct in patients with Meniere's disease. *J Laryngol Otol* 1983;97:1007–12.
14. Nidecker A, Pfaltzb CR, Matéfi L, Benz UF. Computed tomographic findings in Ménière's disease. *ORL* 1985;47:66–75.
15. Yazawa Y, Kitahara M. Computed tomographic findings around the vestibular aqueduct in Meniere' disease. *Acta Otolaryngol* 1991;111:88–90.
16. Krombach GA, van den Boom M, Di Martino E, et al. Computed tomography of the inner ear: size of anatomical structures in the

normal temporal bone and in the temporal bone of patients with Menière's disease. *Eur Radiol* 2005;15:1505–13.
17. Maiolo V, Savastio G, Modugno GC, Barozzi L. Relationship between multidetector CT imaging of the vestibular aqueduct and inner ear pathologies. *Neuroradiol J* 2013;26:683–92.
18. Xenellis J, Vlahos L, Papadopoulos A, Nomicos P, Papafragos K, Adamopoulos G. Role of the new imaging modalities in the investigation of Meniere's disease. *Otolaryngol Head Neck Surg* 2000;123 (1 pt 1):114–9.
19. Inui H, Sakamoto T, Ito T, Kitahara T. Volumetric measurements of the inner ear in patients with Meniere's disease using three-dimensional magnetic resonance imaging. *Acta Otolaryngol* 2016;136: 888–93.
20. Patel VA, Oberman BS, Zacharia TT, Isildak H. Magnetic resonance imaging findings in Ménière's disease. *J Laryngol Otol* 2017;131: 602–7.
21. Sugihara EM, Marinica AL, Vandjelovic ND, et al. Mastoid and inner ear measurements in patients with Menière's disease. *Otol Neurotol* 2017;38:1484–9.
22. Fujita S, Sando I. Three-dimensional course of the vestibular aqueduct. *Eur Arch Otorhinolaryngol* 1996;253:122–5.
23. Watzke D, Bast TH. The development and structure of the otic (endolymphatic) sac. *Anat Rec* 1950;106:361–78.
24. Zehnder AF, Kristiansen AG, Adams JC, Merchant SN, McKenna MJ. Osteoprotegerin in the inner ear may inhibit bone remodeling in the otic capsule. *Laryngoscope* 2005;115:172–7.
25. Donaldson J, Duckert L, Lambert P, Rubel E. In: Anson BJ, Donaldson JA, editors. *Surgical Anatomy of the Temporal Bone. 4th ed.*. New York, NY: Lippincott Williams & Wilkins; 1992.
26. Wilbrand HF, Rask-Andersen H, Gilstring D. The vestibular aqueduct and the para-vestibular canal. An anatomic and roentgenologic investigation. *Acta Radiol Diagn (Stockh)* 1974;15:337–55.
27. Arenberg IK, Rask-Andersen H, Wilbrand H, Stahle J. The surgical anatomy of the endolymphatic sac. *Arch Otolaryngol* 1977;103: 1–11.
28. Nordström CK, Laurell G, Rask-Andersen H. The human vestibular aqueduct: anatomical characteristics and enlargement criteria. *Otol Neurotol* 2016;37:1637–45.